Geophysical Research Letters

RESEARCH LETTER
10.1029/2019GL085600

Heat Content Anomaly and Decay of Warm-Core Rings: the Case of the Gulf of Mexico

Thomas Meunier[1], Julio Sheinbaum[1], Enric Pallàs-Sanz[1], Miguel Tenreiro[1], José Ochoa[1], Angel Ruiz-Angulo[2], Xavier Carton[3], and Charly de Marez[3]

[1]Ensenada Center for Scientific Research and Higher Education, Ensenada, Mexico, [2]Icelandic Meteorological Office, Reykjavik, Iceland, [3]Laboratoire d'Océanographie Physique et Spatiale, Plouzané, France

Key Points:
- The total heat content of 32 Loop Current rings is estimated using altimetry and in situ data
- Their decay rate is inferred and the processes driving it are discussed
- A range of depth-averaged effective lateral diffusivity is proposed for Loop Current rings

Correspondence to:
T. Meunier,
meunier@cicese.mx

Citation:
Meunier, T., Sheinbaum, J., Pallàs-Sanz, E., Tenreiro, M., Ochoa, J., Ruiz-Angulo, A., et al. (2020). Heat content anomaly and decay of warm-core rings: The case of the Gulf of Mexico. *Geophysical Research Letters*, *47*, e2019GL085600. https://doi.org/10.1029/2019GL085600

Received 27 SEP 2019
Accepted 17 JAN 2020
Accepted article online 23 JAN 2020

Abstract In this study, we harness the 25-year satellite-altimeter record, in concert with a vast array of in situ measurements, to estimate the heat content anomaly of 32 warm-core rings in the Gulf of Mexico (GoM). The decay rate of these mesoscale eddies is studied in detail, and it is shown that they release the majority of their heat as they drift in the central GoM (away from topographic obstacles). The surface heat fluxes from the eddies are shown to be small in comparison to the total rate of heat loss from the eddies, suggesting that heat is primarily released toward the surrounding water masses. Integrating the total heat evolution equation over the warm-core rings yields an estimate of their effective lateral diffusivity coefficient. The long-term impact of warm-core rings on heat and salt balance in the GoM is also discussed.

1. Introduction

Warm-core rings are mesoscale, surface-intensified, anticyclonic eddies that commonly detach from intense meandering currents. Famous examples include Kuroshio rings in the North Pacific (Li et al., 1998; Sasaki & Minobe, 2014), Agulhas rings in the South Atlantic (Olson & Evans, 1986; Wang et al., 2016), Gulf Stream rings in the North Atlantic (Liu et al., 2018; Richardson, 1983), and Loop Current rings (LCRs) in the Gulf of Mexico (GoM) (Donohue et al., 2016; Elliott, 1982). Because they are long lived and coherent, these eddies can trap and carry water masses far away from their formation sites (Beron-Vera et al., 2013; Gordon & Haxby, 1990; Wang et al., 2016) and impact the oceanic basins' thermohaline properties.

Of all the aforementioned eddies, LCRs are of particular interest: they detach, drift, and decay in a semienclosed basin for which they are the only source of external water above 1,000 m (subtropical underwater; SUW) (Bunge et al., 2002; Sheinbaum et al., 2002), so that the thermohaline anomalies they carry are crucial to the basin's heat budget and water mass transformation into Gulf Common Water (GCW) (Hamilton et al., 2018). They were also shown to impact the southern United States whether by controlling severe thunderstorm events (Molina et al., 2016) as well as the reinforcement of hurricanes (Shay et al., 2000; Yablonsky & Ginis, 2013) because of the large available heat reservoir they carry.

While timely observational efforts revealed the main characteristics of LCR's thermohaline structures, consisting of a vertically homogeneous temperature anomaly between the surface and 250 m and a saline core between 150 and 400 m (Cooper et al., 1990; Elliott, 1982; Meunier et al., 2018), the time evolution of their structure, and the rate at which the anomalous water mass mixes with the surroundings remains largely unknown. Synoptic estimates of LCR's heat content anomaly (the difference between an eddy's heat content and that of an equivalent volume of Gulf Common Water) and decay would require repeated observations over several months, and the uncertainty of LCR shedding makes the planning of such experiments difficult.

It has been well admitted that LCR's fate is to mix and decay once they reach the western GoM's continental slope (Biggs & Müller-Karger, 1994), although some eddies were shown to suffer considerable erosion before reaching the so-called *eddy graveyard*, possibly through interaction with the neighboring mesoscale turbulence field (Lipphardt et al., 2008). However, so far, no general and systematic estimate of LCR's heat content anomaly, evolution, and decay during their drifting phase has been attempted. Such estimate is crucial for the understanding of the GoM's heat budget, the GCW formation, and LCR-Atmosphere interactions. Of particular importance is the disentangling of heat losses toward the surrounding water and toward the atmosphere. Early studies of Gulf Stream rings emphasized the role of ventilation on the decay of warm-core rings (Dewar, 1987; Evans et al., 1985), and more recent research highlighted the increased air-sea heat exchanges over warm eddies (Chelton & Xie, 2010), including LCRs (Putrasahan et al., 2017).

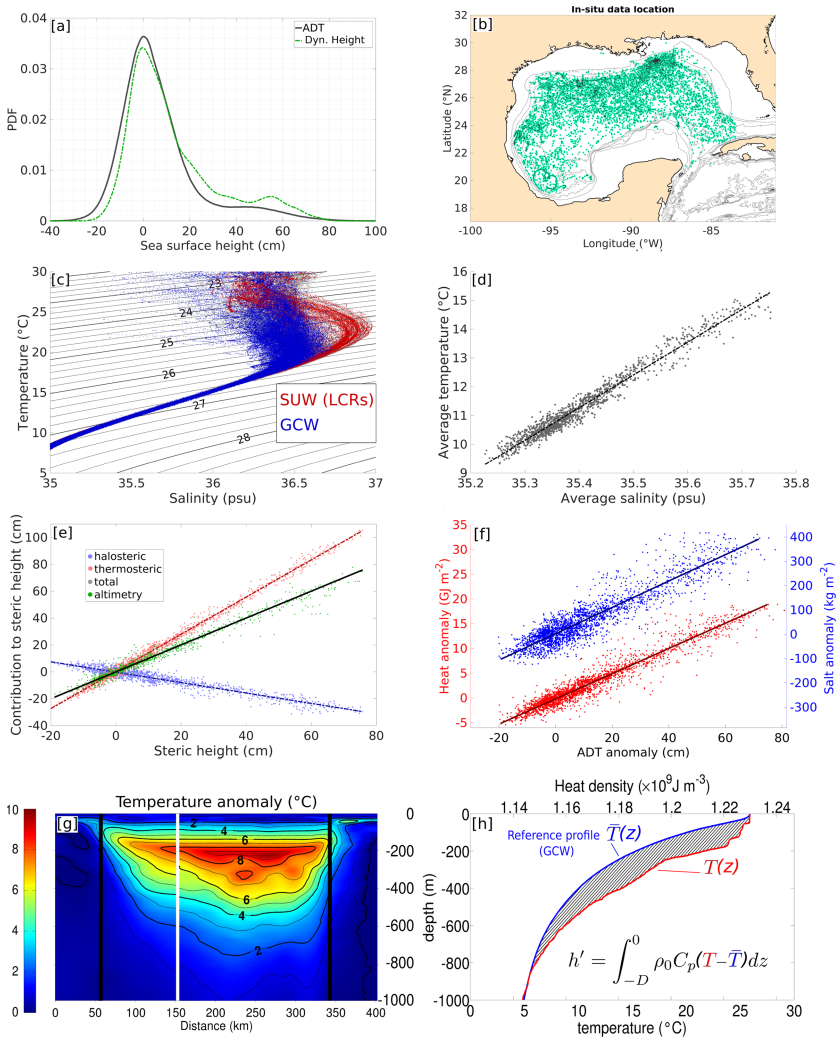

Figure 1. (a) Probability density function of sea surface height in the Gulf of Mexico. The black solid line represents satellite-derived SSH (AVISO absolute dynamic topography, ADT), while the dashed green line represents the dynamic height computed from in situ data. Since the level of reference is arbitrary, both SSH and dynamic height were referenced to the mode of the distribution. (b) Location of the in situ hydrographic profiles. (c) *T*-*S* diagram of the in situ profiles used in the present study. The red dots represent profiles through warm-core rings (subtropical underwater, SUW) while the blue dots represent Gulf Common Water (GCW). (d) Depth averaged *T*-*S* diagram from the surface down to 1,000 dBar. The black solid line represents a linear fit to the data. (e) Thermosteric (red dots) and halosteric (blue dots) contributions to dynamic height (black line). The solid lines represent the linear fits to the data. The green dots represent the corresponding altimeter-derived SSH (Aviso Absolute Dynamic Topography). (f) Heat (red dots) and salt (blue dots) anomalies against sea surface height. The linear fits are plotted as solid lines. (g) Glider section of temperature anomaly across a Loop Current Ring (adapted from ; Meunier et al., 2018, Figure 6b). The thick black vertical lines represent the location of the velocity maxima. (h) Illustration of the LHC computation: the red line represents a random temperature profile accross an eddy while the blue line is the reference GCW profile. LHC is defined as the area between the two curves.

In this paper, we propose an estimate of LCR's total heat content (THC) anomaly and time evolution during the first months of the drifting phase, between 88° and 95°W, before the occurrence of any vortex splitting or merging events. Using simple theoretical arguments, we take advantage of 24 years of satellite altimetry and of a large database of in situ data to infer an empirical relationship between sea surface height (SSH) and local heat content (LHC) anomaly. This allows us to build a climatology of 32 eddies and estimate their THC, decay rate, effective depth-averaged lateral diffusivity, and to infer heat exchanges toward the surrounding ocean and toward the atmosphere.

2. Estimating LCR's Total Heat Content Anomaly and Its Evolution

2.1. Data

All satellite altimetry data used in this work are AVISO Absolute Dynamic Topography. We use 10-day composite products objectively mapped on a 0.25° regular grid. In situ data were obtained from the World Ocean Database and consist of 3,995 validated profiles within the GoM. The selected data are composed of 77% autonomous profiler data (Argo) and 23% ship CTD stations. Assuming that the 40 cm SSH approximately represents the transition between GCW and SUW, 14% of the total in situ database was acquired within LCRs. Figure 1b shows a map of all profiles locations: despite a denser observational effort in the north, the whole Gulf is well sampled. The distribution of satellite altimeter SSH and of in situ computed dynamic height are shown in Figure 1a: both show a well-defined primary mode, corresponding to GCW (SSH = 0), and a smaller secondary mode corresponding to SUW (45 cm < SSH < 55 cm). The slightly larger amplitude of the second mode in dynamic height, compared to altimeter SSH, is most likely due to the important community effort to sample the Loop Current and LCRs. The turbulent heat fluxes (latent and sensible heat fluxes) used in this study are the IFREMER-FLUX data set v4, which is based on the European Space Agency Ocean Heat Flux project. They are calculated as daily estimates with a regular grid spacing of 0.25° (Bentamy et al., 2017).

2.2. Inferring Total Heat Content Anomaly From Altimetry

Satellite measurements of the SSH were shown to be a good proxy for dynamic height (η) in the GoM (Hamilton et al., 2018). The latter is defined as the vertical integral of specific volume anomaly between a given geopotential level and the surface, which, under the hydrostatic approximation is proportional to the vertical integral of density anomaly (Gill & Niiler, 1973):

$$\eta = \frac{1}{\rho_0}\int_{-D}^{0}\rho'(z)\mathrm{d}z, \tag{1}$$

where $\rho_0 = 1,\ 027\ \mathrm{kg/m^3}$ is a reference density, $\rho'(z)$ is density anomaly, defined as the difference between the local instantaneous density profile $\rho(z)$, and a reference density profile $\overline{\rho}(z)$. Here, D is chosen to be the level of no motion (flat reference geopotential surface), assumed to be 1,000 m in the GoM (Oey et al., 2005), so that dynamic height coincides with the 0–1,000 dBar steric height.

In this work, all reference variables, including temperature, salinity, density, and SSH are chosen to be GCW, which we define as the mode of the distribution of each variable. Anomaly is computed as the difference between a given vertical profile and the reference profile, as illustrated in Figure 1h. The vertically averaged values for these reference profiles are 10.7 °C, 35.36 psu, 1,026.95 kg/m^3, and 24 cm, for temperature, salinity, potential density, and satellite-derived SSH, respectively. Satellite-derived SSH is compared to in situ dynamic height in Figure 1e: They are in good agreement, with little scattering about the linear fit (mean absolute error of 4.3 cm).

Under the linear equation of state approximation, density anomaly is a linear combination of temperature (T') and salinity (S') anomalies:

$$\rho' = \rho_0(-\alpha T' + \beta S'), \tag{2}$$

where α and β are the thermal dilatation and haline contraction coefficients, respectively. In the limit of small salinity variations, density anomaly is controlled by temperature anomaly, and the use of SSH anomaly has been shown to be a solid proxy for the LHC anomaly h' above the level of no motion (Willis et al., 2003, 2004):

$$h' = \int_{-D}^{0}\rho_0 C_p T'\mathrm{d}z, \tag{3}$$

$$\eta' \approx \frac{A}{\rho_0 C_p}h', \tag{4}$$

where C_p is the specific heat of sea water and the new variable A is introduced here since α is both temperature and depth dependent:

$$A = \frac{\int_{-D}^{0}\alpha T'}{\int_{-D}^{0}T'}\mathrm{d}z. \tag{5}$$

As evident on the T-S diagram of Figure 1c, the Gulf of Mexico's two main water masses (SUW and GCW) exhibit strong salinity differences, so that the approximation of equation (4) does not hold. However, estimating LHC from altimetry is still possible, provided there exists a linear relationship between the depth-integrated salinity and temperature contributions to density anomaly:

$$\gamma = \frac{\int_{-D}^{0} \beta S' \mathrm{d}z}{\int_{-D}^{0} \alpha T' \mathrm{d}z} = \text{constant}. \tag{6}$$

A depth-averaged T-S diagram of all in situ profiles is shown in Figure 1d: Linearity of the depth-averaged T-S relationship holds for the whole range of water masses found in the GoM. As predicted by equations (1) and (2), linearity of the depth-averaged T-S relationship results in linear variations of the contributions of halosteric and thermosteric effects in dynamic height variations (Figure 1e).

Hence, provided the validity of equation (6) and an empirical value for γ obtained from the in situ database, LHC can be estimated from any SSH field as

$$h' = \frac{\rho_0 C_p}{A(1-\gamma)} \eta'. \tag{7}$$

Assessment of the validity of equation (7) was performed, retrieving γ from the in situ data and using satellite-derived SSH as a proxy for η'. Figure 1f shows local heat (red dots and solid line) and salt (blue dots and solid line) content anomalies against SSH. Linearity of the relationship between LHC and SSH is evident, with a coefficient of determination between in situ data and the linear fit of $R^2 = 0.86$. Salt content anomaly exhibits more scattering, with a coefficient of determination of $R^2 = 0.77$. Note, however, that scattering is larger for high SSH values, with R^2 decreasing to 0.70 when considering SSH greater than 40 cm (SUW) only.

To track LCRs in the 24 years SSH database and compute eddy-integrated variables, it is necessary to choose a dynamically appropriate criterion for the eddy's edge. Here, we are concerned with the trapping and evolution of heat in coherent eddies, so that we should confine ourselves to the eddies core, whose boundary would represent a barrier for tracer exchange in the absence of diffusive processes. This boundary was shown to correspond to a sign change of the Okubo-Weiss parameter (OW) (Elhmaidi et al., 1993; Jeong & Hussain, 1995; Isern-Fontanet et al., 2003, 2004; Okubo, 1970; Weiss, 1991). As shown by Isern-Fontanet et al. (2004), for geostrophic eddies (nondivergent and azimuthal flow) in cylindrical coordinates, $\mathrm{OW} = -4\frac{1}{r}\partial_r(u^2)$ (where r is the radial coordinate and u is the geostrophic velocity), so that the boundary of the core ($\mathrm{OW} = 0$) coincides with the radius of maximum velocity. In this study, we thus defined the eddy's edge C as the maximal circulation contour (the closed SSH contour along which the path-integral of geostrophic velocity is maximal). This contour also coincides with a sign-change of vorticity, so that it encloses the anticyclonic region of the eddies only. This criterion also ensures that the edge contour corresponds to the zone where thermohaline properties have the sharpest gradients, assuring the capture of most of the thermohaline anomalies. This is illustrated in Figure 1g (adapted from Meunier et al., 2018, Figure 6b), which shows a vertical section of temperature anomaly through a Loop Current Ring. The core of anomalously warm water is confined between the velocity maxima (thick black vertical lines). Note that, since the last closed contour is a commonly used criterion for eddies edges in detection algorithms (Chaigneau et al., 2008), the latter is also briefly discussed in this paper for comparison.

The eddy's THC is defined as the surface integral of LHC enclosed within the boundary $C(\theta, t)$:

$$\mathbf{H_e}(t) = \int_0^{2\pi} \int_0^{R(\theta,t)} h_e(\theta, r, t) r \mathrm{d}r \mathrm{d}\theta \tag{8}$$

where the "e" subscripts denote the anomalies associated with the eddy (equivalent to the primed variables in the general case described above), θ is the azimuth, t is time, $R(\theta, t)$ is the radial position of the boundary C, which may vary both with time and azimuth (the eddy is not necessary circular), and $h_e = \int_{-D}^{0} \rho_0 C_p T_e$ is LHC. Temperature T_e is referenced to the mode of the temperature distribution, which corresponds to GCW (vertical profile with a vertically averaged temperature of 10.7 °C).

We also define the eddy's equivalent mean surface flux density as the mean rate of change of THC per unit area:

$$\overline{Q}_e = \frac{\partial_t \mathbf{H_e}}{\mathcal{A}_e}, \tag{9}$$

where $\mathcal{A}_e$ is the eddy's area. $\overline{Q}_e$ has the dimension of a heat flux density (W/m^{-2}) and is a convenient variable to compare the eddies heat loss with the average surface heat flux density.

2.3. Heat Evolution and Effective Lateral Diffusivity

The evolution equation for LHC is obtained by integrating the temperature evolution equation between depth D and the surface:

$$\partial_t h_e + \vec{\nabla} \cdot (h_e \vec{u}_e) = \vec{\nabla} \cdot (K_h \vec{\nabla} h_e) + Q^s_{\text{tot}} - Q^d. \tag{10}$$

$\vec{u}_e$ is the depth-averaged horizontal velocity, $\vec{\nabla}$ is the horizontal component of the Del operator, K_h is the depth-averaged lateral diffusion coefficient, Q^s_{tot} is the total surface heat flux, defined as the sum of the radiative (Q^s_{rad}), latent (Q^s_{lat}), and sensible (Q^s_{sen}) heat fluxes. Q^d is a diffusive heat flux at depth D, defined as $Q^d = K_v \partial_z T_e(D)$, where K_v is the vertical diffusion coefficient and $\partial_z T_e(D)$ is the vertical temperature gradient at depth D. Note that equation (10) is equivalent to Moisan and Niiler's (1998) temperature evolution equation under the assumption of small temporal variations of the depth D, which is valid for large values of D. In the present work, D is the level of no motion, which is assumed to be constant (1,000 m).

Integrating equation (10) over the eddy's surface (defined by the time and azimuth-varying radius $R(\theta, t)$) yields an equation for the evolution of THC:

$$\partial_t \mathbf{H_e}(t) = \frac{1}{2} \int_0^{2\pi} h_e(R) \partial_t R^2 \mathrm{d}\theta + \int_0^{2\pi} \int_0^{R(\theta,t)} \vec{\nabla} \cdot (K_h \vec{\nabla} h_e) r \mathrm{d}r \mathrm{d}\theta + \int_0^{2\pi} \int_0^{R(\theta,t)} (Q^s - Q^d) r \mathrm{d}r \mathrm{d}\theta. \tag{11}$$

Since integration is done along closed stream lines, the heat flux divergence term vanishes. The first term on the right-hand side arises from Leibnitz's theorem on integration over variable intervals and is related to geometrical variations of the eddy's edge (mostly related to geostrophic readjustment during the eddy's decay). It will be referred to as the spreading term. Using the two-dimensional Ostrogradski theorem and assuming that K_h is homogeneous along the edge contour of the eddy, the surface integral of the lateral diffusion term (second term on the right-hand side of equation (11)) can be rewritten:

$$\iint_S \vec{\nabla} \cdot (K_h \vec{\nabla} h_e) \mathrm{d}S = K_h(R) \oint_C \vec{\nabla} h_e \cdot \vec{n} \mathrm{d}c, \tag{12}$$

where $K_h(R)$ is the mixing coefficient at the edge of the eddy, $\vec{n}$ is a unit vector normal to the contour C, and dc is a contour element.

Neglecting Q^d, equation (11) immediately yields an effective depth-averaged lateral diffusivity coefficient :

$$K_h(R) = \frac{\partial_t \mathbf{H_e}(t) - \frac{1}{2} \int_0^{2\pi} h_e(R) \partial_t R^2 \mathrm{d}\theta - \int_0^{2\pi} \int_0^{R(\theta,t)} (Q^s_{tot}) r \mathrm{d}r \mathrm{d}\theta}{\oint_C \vec{\nabla} h_e . \vec{n} \mathrm{d}c} \tag{13}$$

In practice, turbulent diffusivity can be defined as the ratio of the covariance of small-scale velocity and LHC fluctuations and the mean LHC gradient of the mesoscale eddy:

$$K_h = \frac{\overline{\vec{u'}_e h'_e}}{\vec{\nabla} \overline{h}_e}. \tag{14}$$

The K_h estimates proposed in this work are effective diffusivity coefficient and represent the advective effects of all subgridscale fluctuations of velocity $\vec{u'}_e$ and LHC h'_e, including submesoscale turbulence surrounding the eddies, or intrinsic high azimuthal wave number instability of the eddies.

3. Results

3.1. LCR's Total Heat Content Anomaly and Its Evolution

Between 1 January 1993 and 1 January 2017, 32 LCRs were identified and tracked. Their edge contour, 10 days after detachment are shown in a centered frame of reference in Figure 2a. The LCRs have a wide size range, with radii ranging between 87 and 178 km and areas between 2,400 and 9,900 km^2. Figure 2a also clearly shows a correlation between LCR's sizes and SSH: the larger the LCR, the larger the mean SSH. LCRs detach between 25 and 27.4°N, and their general southwestward path keeps covering a meridional range of

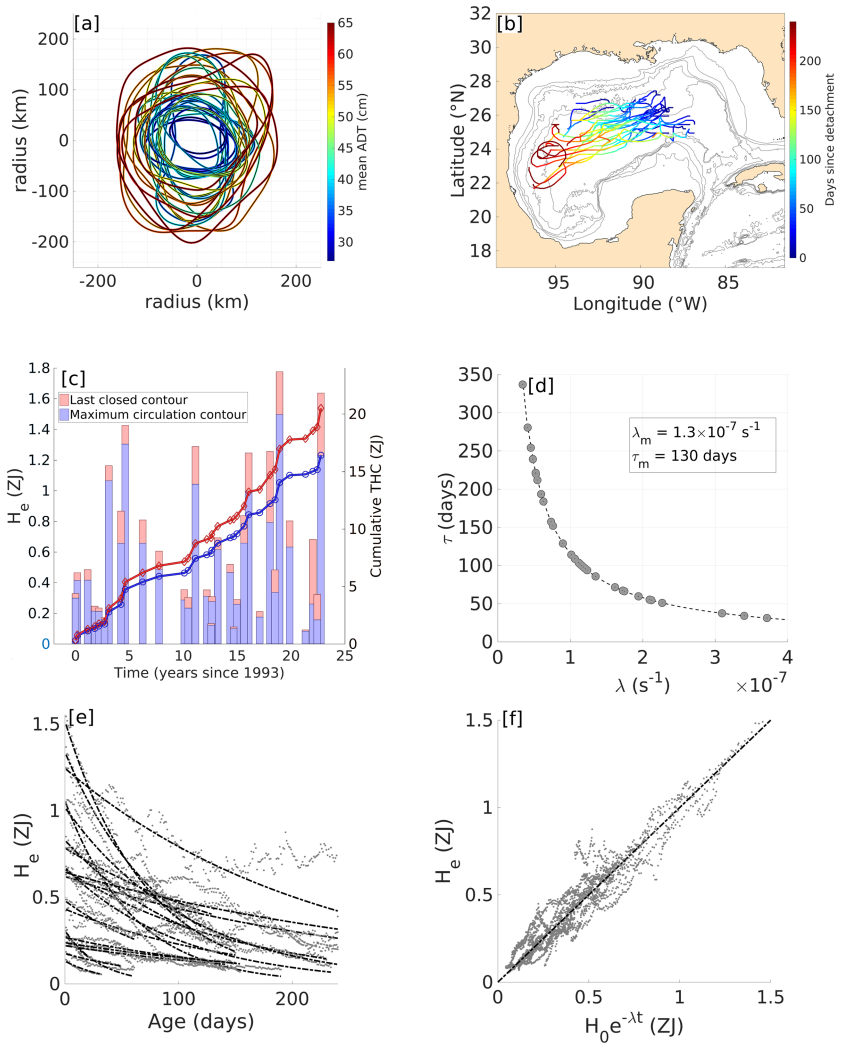

Figure 2. (a) Centered edge contours of the 32 LCEs 10 days after detachment. The mean SSH of each eddy is color coded. (b) Trajectory of the center of the 32 LCEs. The eddy's age (time since detachment) is color coded. (c) Heat content anomaly of each detached eddy 10 days after detachment. Values computed using the maximal circulation contours are shown as blue bars, while those computed using the last closed contours are plotted in red. The cummulative heat for both cases is represented by the blue and red solid lines. (d) *e*-folding time τ against decay rate λ for all detected LCRs (gray dots). The dashed line is the $\lambda = 1/\tau$ function. (e) Time evolution of the eddies heat content anomaly (gray dots). Exponential decay fits are superimposed as dashed black lines. (f) Heat content anomaly of the eddies against the exponential fits (gray dots).The dashed black line represents the linear regression to the data.

approximatively 2° (Figure 2b). The eddies were tracked for periods ranging from 30 to 240 days, with an average tracking time of 150 days. Note that the tracking time does not necessarily coincide with the eddy's full life time, since tracking ended at the first splitting or merging event.

The cumulative heat contained in the 32 LCRs, as well as their individual heat content anomaly 10 days after detachment, are shown in Figure 2c. The blue line represents values computed using the maximal circulation contour criterion, while the red line represents the last closed contour criterion case. Between 1993 and 2017, LCRs carried 16.5 ZJ (1 ZJ $= 10^{21}$ J) toward the interior GoM (20.4 ZJ when considering the last closed contour as the outer edge of the eddies). The individual THC of each eddy 10 days after detachment is highly variable, ranging between 0.08 and 1.6 ZJ, for an average of 0.51 ZJ (0.63 ZJ when considering the last closed contour as the outer edge of the eddies) .

Figure 2e shows time series of LCR's THC during their drift. After detachment, THC decays exponentially with time. A decay law of the form $\mathbf{H_e}(t) = \mathbf{H_e}(0)e^{-\lambda t}$ was fitted to the time series. Values for the decay rates

λ of each eddy were computed as

$$\lambda = \langle -\frac{\ln(\mathbf{H_e}(t)/\mathbf{H_e}(0))}{t} \rangle_T, \tag{15}$$

where $\langle\cdot\rangle_T$ is the time-mean operator. Time series of the fitted exponential decay are superimposed on time series of observed THC in Figure 2e, while they are plotted against each other in Figure 2f. On average, the exponential decay law is a good approximation of THC, with a mean relative error of 15%. Figure 2d shows the range of decay rate and corresponding *e*-folding decay time ($\tau = \lambda^{-1}$) for the 32 LCRs. Decay rates are highly variable, with a range spanning 1 order of magnitude ($3.4 \times 10^{-8} < \lambda < 3.7 \times 10^{-7}$ s^{-1}), yielding an average *e*-folding time of 130 days, and a range between 30 and 340 days.

3.2. Impact of the Surface Heat Fluxes

To quantify and understand the effects of surface fluxes in the eddies decay, the eddies equivalent mean surface flux density ($\overline{Q}_e$) were computed following equation (9). The distribution of $\overline{Q}_e$ is compared to the eddy-averaged radiative ($\overline{Q}^s_{\text{rad}}$), turbulent ($\overline{Q}^s_{\text{turb}}$), and net total ($\overline{Q}^s_{\text{tot}}$) heat flux density in the histogram of Figure 3a. The net total heat flux density has a near-zero mean (5 W/m^2), because of the compensating contributions of turbulent and radiative heat fluxes, which have average values of −140 and 145 W/m^2, respectively. Although the distribution of $\overline{Q}_e$ overlaps the distribution of the total surface heat flux density, on average, the eddies lose heat at a much faster rate than surface heat fluxes would cause, with an average value of $\overline{Q}_e = -490$ W/m^2, and extreme values reaching −2,000 W/m^2.

To infer the possible seasonality of the eddies heat loss, monthly mean values of $\overline{Q}_e$ were computed. They are shown in Figure 3b and compared with monthly means of $\overline{Q}^s_{\text{tot}}$, $\overline{Q}^s_{\text{turb}}$, and $\overline{Q}^s_{\text{rad}}$. While the seasonal cycle of the surface heat fluxes is clear, with $\overline{Q}^s_{\text{tot}}$, $\overline{Q}^s_{\text{turb}}$, and $\overline{Q}^s_{\text{rad}}$ varying respectively from −145, −210, and 65 W/m^{-2} in December to 150, −70, and 220 W/m^2 in June, no evident cycle is discernible in the monthly $\overline{Q}_e$ variations. Moreover, maximum eddy heat loss is found to occur in July and August (average of −770 and −800 W/m^{-2}, respectively), which is a period of positive total net surface heat flux (heat gain for the eddies).

The radial distribution of the time variation of the eddies LHC ($\partial_t h_e(r)$) was also investigated, computing azimuthally averaged radial mean profiles for each eddy. A composite profile was computed as the average of all eddies, nondimensionalizing the radial coordinate with each eddy's radius. The mean radial distribution of surface heat flux density (Q^s_{tot}, Q^s_{turb}, and Q^s_{rad}) was computed following the same method. Results are shown in Figure 3d. The radial distribution of $\partial_t h_e(r)$ has a Gaussian form, with a maximum value of 550 W/m^2 near the eddy's center, decreasing to zero at $r = 2$, and changing sign to reach moderate positive values (60 W/m^2) at $r = 3$. Despite enhanced turbulent fluxes over the eddies (−165 W/m^2 at $r = 0$ and −125 W/m^2 at $r = 2$), the total surface heat flux density remains small (between 0 and +20 W/m^2), because of the compensating contributions of turbulent and radiative heat fluxes when averaged over the life times of the 32 eddies.

To assess the long-term effect of surface fluxes on the eddies, the total heat loss caused by surface heat fluxes during the eddies tracking period was computed as the integral of the surface heat flux density over the surface of each eddy from detachment to the end of the detection period (before splitting or merging):

$$H_{surf} = \int_0^T \int_0^{2\pi} \int_0^R Q^s_{tot} r \mathrm{d}r \mathrm{d}\theta \mathrm{d}t, \tag{16}$$

where T is the time during which each eddy was tracked. The ratio of H_{surf} and the eddies total loss during time T ($H_{\text{surf}}/(\mathbf{H_e}(0) - \mathbf{H_e}(T))$) was computed and its distribution is shown in Figure 3c. The ratio ranges between −18 and 26% and has a near zero-mean ($\approx -1\%$), showing that the net effect of surface heat fluxes on a LCR life cycle can be a heat gain as well as a heat loss, and that, in any case, its impact is moderate.

3.3. Effective Lateral Diffusivity Estimates

Effective lateral diffusivity coefficients K_h were computed for all eddies using equation (13). Their distribution is shown on the histogram of Figure 3e. The average value of K_h is 215 m^2/s^1, but the distribution exhibits a wide range of variations, eventually reaching 1,500 m^2/s^1, and including events of negative values. Obviously, negative diffusivity coefficients K_h do not have any physical meaning, and are an artifact of the methods. Here, occurrence of negative K_h is associated with short events of THC increase that are not compensated by an increase of the surface heat fluxes or the spreading term.

To assess the time evolution of the diffusivity coefficient as the eddies drift, the diffusivity coefficient of the 32 LCRs and the different terms of equation (13) were averaged over 10-day time intervals from their

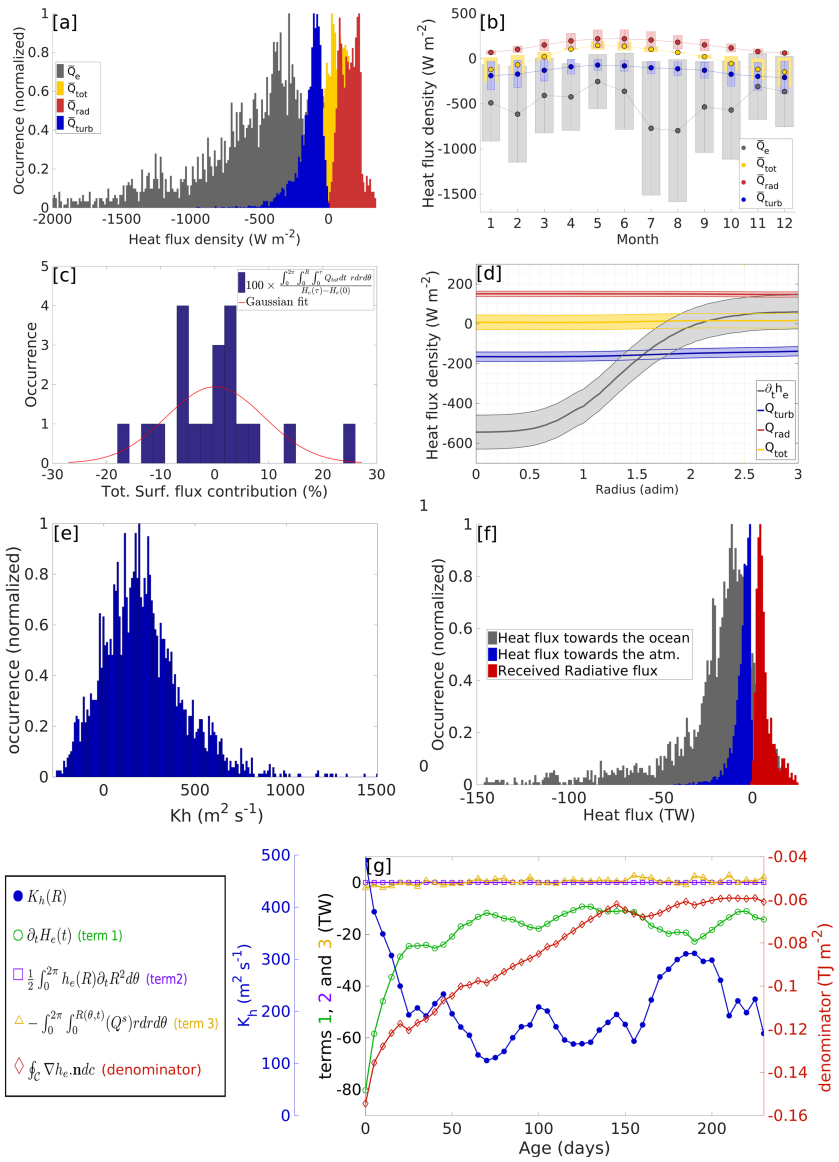

Figure 3. (a) Distribution of eddy-averaged rate of heat loss (gray bars), total surface heat flux density (yellow bars), radiative surface heat flux density (red bars), and turbulent surface heat flux density (blue bars). (b) Monthly means of eddy-averaged rate of heat loss (gray dots), total surface heat flux density (yellow dots), radiative surface heat flux density (red dots), and turbulent surface heat flux density (blue dots). The standard deviations are plotted as light color bars. (c) Distribution of the contribution of the total surface heat flux to the eddy's heat loss (blue bars). The red line represents a Gaussian fit. (d) Composite radial distribution of the eddy's rate of heat loss (gray line), total surface heat flux density (yellow line), radiative surface heat flux density (red line), and turbulent surface heat flux density (blue line). The shaded areas represent the standard deviation between the observed eddies. (e) Distribution of the depth-averaged effective lateral diffusivity coefficient (K_h). (f) Distribution of the heat flux toward the surrounding ocean (diffusive flux, gray bars), heat flux toward the atmosphere (turbulent surface flux and upward long-wave radiation), and the radiative heat flux received by the eddy (downward short and long wave radiations). (g) Time evolution of the mean K_h (blue line and dots), and of the different terms in equation (13).

detachment until the end of the tracking period. As shown in Figure 3g, K_h is maximal right after detachment, and then decreases from 500 to 120 m^2/s during the first 2 months. It then fluctuates between 100 and 300 m^2/s^1 during the rest of the tracking periods, as the number of observations starts to decrease. Sensitivity tests on the averaging time interval were performed (not shown), showing a decrease of the initial K_h values and a smoothing of the fluctuations when increasing the interval. The rapid decrease of K_h during the early life stage of the eddies is associated with a rapid decrease of the eddies rate of heat loss $\partial_t \mathbf{H_e}$ (first term of equation (13)), and a continuous decrease of the radial component of the LHC gradient integrated over

the eddy's edge contour (denominator in equation (13)). The surface heat flux and spreading terms (Terms 2 and 3 in equation (13)) remain small and do not affect the evolution of K_h with time.

Estimating and comparing heat transfers toward the atmosphere and toward the surrounding ocean is of particular interest. In our framework, the only heat flux from the eddies toward the ocean is the diffusive heat flux, which represents the advective effects of all unresolved fluctuations (second term on the right-hand side of equation (11)). Heat is transfered from the eddies toward the atmosphere through turbulent heat fluxes and upward long-wave radiative fluxes. The total heat fluxes distributions are shown in Figure 3f. The total heat flux of LCRs toward the atmosphere ranges between 0.2 and 30 TW, with an average value of 5.6 TW, while the total heat received by an eddy through solar radiation has an average 5.7 TW, which compensates the eddies losses toward the atmosphere. In comparison, the total heat flux toward the ocean (diffusive flux) is large, with an average value of 21 TW, eventually reaching 150 TW for some particularly large eddies during their early life cycle.

4. Discussion and Conclusion

In this observational study, we gave a quantitative estimate of the THC of all LCRs detached between 1993 and 2017 and described their exponential decay as they drift through the central GoM. We showed that total net surface heat fluxes could not account for the fast heat loss of the eddies, and that lateral mixing was therefore necessarily a key process to explain the observed decay rates. Using simple theoretical arguments, we proposed an estimate of the effective lateral diffusivity coefficient, representing the effects of all subgrid processes (at scales smaller than 0.25°).

Beyond numbers, this study aims to bring a better understanding of the heat budget in the GoM and the processes controlling LCRs erosion. In particular, it is of interest to discuss the fate of the total heat carried into the inner GoM by LCRs and its implication for the basin's heat budget. The residual net annual surface heat fluxes over the GoM are still subject to debate, with estimates ranging between −24 and 46 W/m^2 (Zavala-Hidalgo et al., 2002). To keep the GoM's total heat content stationary between 1993 and 2017 despite the 16.5 ZJ carried by LCRs, the necessary average residual surface heat flux over its 1.6×10^6 km^2 area ($\mathcal{A}_{\mathrm{GoM}}$) can be estimated as

$$Q_{\mathrm{res}} = \frac{\sum_{n=1}^{32} \mathbf{H}_{\mathbf{e}}^{n}}{\mathcal{A}_{\mathrm{GoM}} \Delta t}, \tag{17}$$

where $\sum_{n=1}^{32} \mathbf{H}_{\mathbf{e}}^{n}$ is the total heat carried by the 32 eddies during the time interval $\Delta t = 24$ years. The average residual surface heat flux is found here to be a net heat loss of 14 W/m^{-2}, similar to Hastenrath's (1968) estimate, but less than Etter, 's (1983) 25 W/m^2. Since several authors suggested that residual net surface heat fluxes were near-zero or a heat gain for the GoM (Adem et al., 1993; Zavala-Hidalgo et al., 2002), it is interesting to estimate the impact of unbalanced LCRs heat input. Under the approximation of a long-term homogeneous redistribution of LCR's heat excess over the whole GoM's surface, equation (7) predicts that, in the case of a zero annual mean net flux, the mean sea level would have increased by 66 cm in 24 years, which has not been observed. This supports the existence of a yearly residual negative surface heat flux over the GoM.

Although this study is focused on heat, similar estimates are possible for the salt content anomaly. Combining equations (1), (2), and (6), a similar expression to equation (8) describes the total salt content anomaly of LCRs :

$$\mathbf{S_e} = \int_0^{2\pi} \int_0^{R(\theta,t)} \int_{-D}^{0} \frac{\eta'}{\beta(1-\gamma^{-1})} r \mathrm{d}r\mathrm{d}\theta \tag{18}$$

Applying this expression to the LCR database, we find an average total salt content anomaly of 10.7 billion tons and a cumulative salt excess of 342 billion tons for the GoM between 1993 and 2017. The fresh water input necessary to keep a mean salinity of $\overline{S} = 35.4$ psu in the GoM can be estimated as

$$F = \frac{\sum_{n=1}^{32} \mathbf{S_e^n}}{\overline{S} \Delta t}. \tag{19}$$

Numeric values for $\sum_{n=1}^{32} \mathbf{S_e^n}$ described above yield a necessary freshwater input of 12,700 m^3/s, which closely match Morey et al., 2003's (2003's) recent estimates of the Mississipi discharge (13,000 m^3/s) and is slightly larger than the total freshwater input estimates of Elliott (1982) (11,000 m^3/s).

Our estimates of decay rate and *e*-folding times give interesting information on where LCR's heat is released. From the 32 eddies, 9 were tracked until they approached the western GoM's shelf. The average time for those eddies to reach the longitude of 95°W is 190 days, while the average *e*-folding decay time τ is 130 days. After time τ, an eddy's THC is $\frac{\mathbf{H_e}(0)}{e^1}$, which suggests that in average, eddies have lost nearly 2/3 of their heat two months before they reach the eddy graveyard. This study thus shows that on average, eddies primarily release their heat toward the interior GoM, and that they have considerably decayed as they reach the western GoM.

One important result of this study is the seemingly secondary role played by surface heat fluxes in the eddies decay: Although on average, turbulent heat fluxes extract heat to LCRs at a rate corresponding to about 35% of the total eddy's heat loss, the latter are compensated by the heat gained from radiative heat fluxes, so that the average effect of total surface heat fluxes is close to zero. Heat fluxes may however have an indirect impact on the LCRs heat loss: using a $1_{1/2}$-layer model of a zero-potential vorticity warm-core ring, Dewar (1987) showed that warm-core rings decayed through ventilation was not only related to the direct heat loss toward the atmosphere, but that secondary processes, including geostrophic readjustment, resulted in large amount of energy loss in the internal-wave spectrum. The applicability of Dewar, 's (1987) theoretical model seems however limited in our case: while the $1_{1/2}$-layer model seems suited to describe LCRs, and the zero-potential vorticity hypothesis, despite not being representative of LCRs, may be acceptable; the magnitude of instantaneous heat losses considered by Dewar (1987) are extremely far from what is observed in the GoM. Considering the extreme case of a 12-hr cold-front event, where latent heat fluxes can reach 1,000 W/m^2 and radiative fluxes tend to zero, the total heat loss toward the atmosphere can be approximated as

$$\Delta \mathbf{H_e} = \int_0^{12h} \int_0^{2\pi} \int_0^{R(\theta,t)} Q_{lat}^s r dr d\theta dt. \tag{20}$$

For an average LCR, the ratio $\Delta \mathbf{H_e}/\mathbf{H_e}$ has a value of 0.27%, which is 2 orders of magnitude smaller than the most moderate case considered by Dewar (1987) (20%). It is also important to note that the heat loss would occur continuously during 12 hr, which is half the inertial period at 25°N, so that it can hardly be considered as instantaneous. Since the magnitude of the effects of adjustment on the eddy's decay is directly linked to this instantaneous heat loss ratio, one could argue that it should have small effects in our case. Moreover, important adjustment should result in a large spreading term, which is not observed here (Figure 3g).

That most of LCRs' heat is transfered to the surrounding water rather than toward the atmosphere is an unexpected result. However, it is important to keep in mind that even if the atmosphere has relatively moderate effects on LCRs, the latter have strong impact on extreme mesoscale atmospheric events, such as thunderstorm cells (Molina et al., 2016) and hurricanes (Shay et al., 2000), that strongly affect human activity. In that regard, our results do not aim to lessen the importance of air-sea fluxes over LCRs. We simply suggest that air-sea fluxes have a more relative importance for the atmosphere than for LCRs life cycle.

It is also important to note that all heat flux products have a large error in the GoM, which is one of the world's region with most uncertainty in latent heat flux estimates (Bentamy et al., 2017), with errors eventually reaching 60 W/m^2. Although this error may seem large, it is moderate in regard to the large difference between the rate of heat loss of LCRs and the total net heat fluxes (Figures 3a–3d). Propagating an uncertainty of 60 W/m^2 on Q_{tot}^s in equation (13) adds an uncertainty of 13% on the K_h values.

The average lateral diffusivity coefficient estimated in this study (215 m^2/s) is of the same order of magnitude as Joyce and Stalcup's (1985) estimates in Gulf Stream rings (200–500 m^2/s), which are close cousins of LCRs, but more than Olson, 's (1986) 90 m^2/s and Chassignet et al., (1990)'s 50 m^2/s in that same type of eddies. Our results are also close to Conway et al., (2018)'s and Qiu et al., (2007)'s estimate in a Kuroshio ring (300 m^2/s). They are however significantly larger than Ledwell et al., (2008)'s estimates in Sargasso sea mode water eddies (20 m^2/s). Although extensive field work and numerical experiments have recently provided important information on the dispersion of tracers in the deep GoM (Ledwell et al., 2016), to the best of our knowledge, no estimate of lateral diffusivity is available for LCRs so that a strict comparison of our results with previous work is not possible. It is, however, important to note that the coarse resolution of the

altimetry data might lead to an overestimate of K_h: the radial LHC gradient, which controls the denominator of equation (13), is considerably smoothed on the altimetry grid. While typical velocity maxima found using altimetry are of 0.7 m^2/s, in situ measurements show values ranging between [1 and 2] m^2/s (Cooper et al., 1990; Guan et al., 2011; Meunier et al., 2018). Since surface geostrophic velocity is proportional to the radial SSH gradient, and thus the radial LHC gradient (equation (7)), an underestimation of a factor 2 in surface velocity corresponds to an overestimation of the same factor for K_h. Our average K_h would then be $\approx$100 m^2/s.

Making sense of lateral diffusivity coefficient values can be delicate. Since the latter are extremely dependent on the resolved spatial scale (Shcherbina et al., 2015), the range of values proposed here is only strictly comparable with estimates performed on the same spatial scale. They cannot be directly compared to the results of most dye experiments which are valid for scales of [1–10 km] and yield typical K_h values of O(1 m^2/s) (Ledwell et al., 1998), nor basin-scale experiments, which are valid for scales of [100–1,000 km] and yield typical values of $O(10^4$ m^2/s (Zhurbas & Oh, 2004).

These diffusivity coefficients, which represent the advective effects of subgrid fluctuations, could however be useful for the parameterization of numerical models with similar grid scales (mesoscale permitting but not resolving) such as modern coupled climate models.

While our study cannot shed light on the physical processes responsible for the lateral dispersion of LCR's heat, it clearly shows that these processes occur at the submesoscale (smaller than the smaller scale resolved by SSH, i.e., roughly $2 \times 0.25°$), and that most of LCR's erosion occurs in the interior GoM and not along the western shelf and slope, as previously accepted. An ongoing series of glider surveys in the central GoM, as well as very-high resolution modeling in idealized and regional configurations, should shed light on the details of the processes occuring at O(1–10 km) and impacting heat dispersion. A similar study, applied to Agulhas rings is also in progress, and should extend these results to a different class of eddies, with the purpose of better understanding the role of warm-core rings in the global tracer transport and diffusion at basin scales.

Acknowledgments
This research is funded by the National Council of Science and Technology of Mexico-Mexican Ministry of Energy-Hydrocarbon Trust, project 201441. This is a contribution of the Gulf of Mexico Research Consortium (CIGoM). Absolute dynamic topography products were produced and distributed by the Copernicus Marine and Environment Monitoring Service (CMEMS) (http://www.marine.copernicus.eu). The data set used in this work is the global multisatellite merged product l4-v3 (duacs-rep-global-merged-allsat-phy-l4-v3). In situ temperature and salinity profiles were retrieved from the World Ocean Database (https://www.nodc.noaa.gov/OC5/WOD/pr_wod.html). The majority of these profiles were collected and made freely available by the International Argo Program and the national programs that contribute to it (http://www.argo.ucsd.edu, http://argo.jcommops.org). The Argo Program is part of the Global Ocean Observing System. Ifremer heat fluxes are publically available and can be retrieved at this site (ftp://o1ef56:DeJd6uNv@eftp.ifremer.fr/oceanheatflux/data/third-party/fluxes/ifremerflux_v4/).

References

Adem, J., Villanueva, E., & Mendoza, V. (1993). A new method for estimating the seasonal cycle of the heat balance at the ocean surface, with application to the Gulf of Mexico. *Geofisica Internacional*, *32*(1), 21–34.

Bentamy, A., Piollé, J. F., Grouazel, A., Danielson, R., Gulev, S., Paul, F., & Josey, S. A. (2017). Review and assessment of latent and sensible heat flux accuracy over the global oceans. *Remote Sensing of Environment*, *201*, 196–218. https://doi.org//10.1016/j.rse.2017.08.016

Beron-Vera, F. J., Wang, Y., Olascoaga, M. J., Goni, G. J., & Haller, G. (2013). Objective detection of oceanic eddies and the Agulhas leakage. *Journal of Physical Oceanography*, *43*, 1426–1438. https://doi.org//10.1175/JPO-D-12-0171.1

Biggs, D. C., & Müller-Karger, F. E. (1994). Ship and satellite observations of chlorophyll stocks in interacting cyclone-anticyclone eddy pairs in the western Gulf of Mexico. *Journal of Geophysical Research*, *99*, 7371–7384. https://doi.org//10.1029/93JC02153

Bunge, L., Ochoa, J., Badan, A., Candela, J., & Sheinbaum, J. (2002). Deep flows in the Yucatan Channel and their relation to changes in the Loop Current extension. *Journal of Geophysical Research*, *107*(C12), 3233. https://doi.org//10.1029/2001JC001256

Chaigneau, A., Gizolme, A., & Grados, C. (2008). Mesoscale eddies off Peru in altimeter records: Identification algorithms and eddy spatio-temporal patterns. *Progress in Oceanography*, *79*, 106–119. https://doi.org//10.1016/j.pocean.2008.10.013

Chassignet, E. P., Olson, D. B., & Boudra, D. B. (1990). Motion and evolution of oceanic rings in a numerical model and in observations. *Journal of Geophysical Research*, *95*(C12), 22,121–22,140. https://doi.org//10.1029/JC095iC12p22121

Chelton, D. B., & Xie, S. P. (2010). Coupled ocean-atmosphere interaction at oceanic mesoscales. *Oceanography*, *23*(4), 52–69.

Conway, T. M., Palter, J. B., & de Souza, G. F. (2018). Gulf Stream rings as a source of iron to the North Atlantic subtropical gyre. *Nature Geoscience*, *11*(8), 594–598. https://doi.org//10.1038/s41561-018-0162-0

Cooper, C., Forristall, G. Z., & Joyce, T. M. (1990). Velocity and hydrographic structure of two Gulf of Mexico warm-core rings. *Journal of Geophysical Research*, *95*, 1663–1679. https://doi.org//10.1029/JC095iC02p01663

Dewar, W. K. (1987). Ventilating warm rings: Theory and energetics. *Journal of Physical Oceanography*, *17*, 2219–2231. https://doi.org//10.1175/1520-0485(1987)017<2219:VWRTAE>2.0.CO;2

Donohue, K. A., Watts, D. R., Hamilton, P., Leben, R., & Kennelly, M. (2016). Loop Current eddy formation and baroclinic instability. *Dynamics of Atmospheres and Oceans*, *76*, 195–216. https://doi.org//10.1016/j.dynatmoce.2016.01.004

Elhmaidi, D., Provenzale, A., & Babiano, A. (1993). Elementary topology of two-dimensional turbulence from a Lagrangian viewpoint and single-particle dispersion. *Journal of Fluid Mechanics*, *257*, 533–558. https://doi.org//10.1017/S0022112093003192

Elliott, B. A. (1982). Anticyclonic rings in the Gulf of Mexico. *Journal of Physical Oceanography*, *12*, 1292–1309. https://doi.org//10.1175/1520-0485(1982)012<1292:ARITGO>2.0.CO;2

Etter, P. C. (1983). Heat and freshwater budgets of the Gulf of Mexico. *Journal of Physical Oceanography*, *13*, 2058–2069. https://doi.org//10.1175/1520-0485(1983)013<2058:HAFBOT>2.0.CO;2

Evans, R. H., Baker, K. S., Brown, O. B., & Smith, R. C. (1985). Chronology of warm-core ring 82B. *Journal of Geophysical Research*, *90*, 8803–8811. https://doi.org//10.1029/JC090iC05p08803

Gill, A. E., & Niiler, P. P. (1973). The theory of the seasonal variability in the ocean. *Deep Sea Research and Oceanographic Abstracts*, *20*, 141–177. https://doi.org//10.1016/0011-7471(73)90049-1

Gordon, A. L., & Haxby, W. F. (1990). Agulhas eddies invade the South Atlantic: Evidence from Geosat altimeter and shipboard conductivity-temperature-depth survey. *Journal of Geophysical Research*, *95*, 3117–3125. https://doi.org//10.1029/JC095iC03p03117

Guan, X. A., Brown, A., & Brown, A. (2011). On the eddy structure in the Northern Gulf of Mexico—Implications of VMADCP observations from 2005 to 2007. In *Offshore Technology Conference*.
Hamilton, P., Leben, R., Bower, A., Furey, H., & Pérez-Brunius, P. (2018). Hydrography of the Gulf of Mexico using autonomous floats. *Journal of Physical Oceanography*, *48*, 773–794. https://doi.org//10.1175/JPO-D-17-0205.1
Hastenrath, S. L. (1968). Estimates of the latent and sensible heat flux for the Caribbean Sea and the Gulf of Mexico. *Limnology and Oceanography*, *13*, 322–331. https://doi.org//10.4319/lo.1968.13.2.0322
Isern-Fontanet, J., Font, J., García-Ladona, E., Emelianov, M., Millot, C., & Taupier-Letage, I. (2004). Spatial structure of anticyclonic eddies in the Algerian basin (Mediterranean Sea) analyzed using the Okubo Weiss parameter. *Deep Sea Research Part II: Topical Studies in Oceanography*, *51*(25-26), 3009–3028. https://doi.org//10.1016/j.dsr2.2004.09.013
Isern-Fontanet, J., García-Ladona, E., & Font, J. (2003). Identification of marine eddies from altimetric maps. *Journal of Atmospheric and Oceanic Technology*, *20*(5), 772. https://doi.org//10.1175/1520-0426(2003)20<772:IOMEFA>2.0.CO;2
Jeong, J., & Hussain, F. (1995). On the identification of a vortex. *Journal of Fluid Mechanics*, *285*, 69–94. https://doi.org//10.1017/S0022112095000462
Joyce, T. M., & Stalcup, M. C. (1985). Wintertime convection in a gulf stream warm core ring. *Journal of Physical Oceanography*, *15*, 1032–1042. https://doi.org//10.1175/1520-0485(1985)015<1032:WCIAGS>2.0.CO;2
Ledwell, J. R., He, R., Xue, Z., DiMarco, S. F., Spencer, L. J., & Chapman, P. (2016). Dispersion of a tracer in the deep Gulf of Mexico. *Journal of Geophysical Research: Oceans*, *121*, 1110–1132. https://doi.org//10.1002/2015JC011405
Ledwell, J. R., McGillicuddy, J., Dennis, J., & Anderson, L. A. (2008). Nutrient flux into an intense deep chlorophyll layer in a mode-water eddy. *Deep Sea Research Part II: Topical Studies in Oceanography*, *55*, 1139–1160. https://doi.org//10.1016/j.dsr2.2008.02.005
Ledwell, J. R., Watson, A. J., & Law, C. S. (1998). Mixing of a tracer in the pycnocline. *Journal of Geophysical Research*, *103*(C10), 21,499–21,529. https://doi.org//10.1029/98JC01738
Li, L., Nowlin, W. D., & Jilan, S. (1998). Anticyclonic rings from the Kuroshio in the South China Sea. *Deep Sea Research Part I: Oceanographic Research Papers*, *45*(9), 1469–1482.
Lipphardt, B., Poje, A., Kirwan, A., Kantha, L., & Zweng, M. (2008). Death of three Loop Current rings. *Journal of Marine Research*, *66*(1), 25–60.
Liu, Y., Wilson, C., Green, M. A., & Hughes, C. W. (2018). Gulf stream transport and mixing processes via coherent structure dynamics. *Journal of Geophysical Research: Oceans*, *123*, 3014–3037. https://doi.org/10.1002/2017JC013390
Meunier, T., Pallás-Sanz, E., Tenreiro, M., Portela, E., Ochoa, J., Ruiz-Angulo, A., & Cusí, S. (2018). The vertical structure of a Loop Current eddy. *Journal of Geophysical Research: Oceans*, *123*, 6070–6090. https://doi.org//10.1029/2018JC013801
Moisan, J. R., & Niiler, P. P. (1998). The seasonal heat budget of the North Pacific: Net heat flux and heat storage rates (1950-1990). *Journal of Physical Oceanography*, *28*, 401–421. https://doi.org//10.1175/1520-0485(1998)028<0401:TSHBOT>2.0.CO;2
Molina, M., Timmer, R., & Allen, J. (2016). Importance of the Gulf of Mexico as a climate driver for US severe thunderstorm activity. *Geophysical Research Letters*, *43*, 12,295–12,304. https://doi.org/10.1002/2016GL071603
Morey, S. L., Martin, P. J., O'Brien, J. J., Wallcraft, A. A., & Zavala-Hidalgo, J. (2003). Export pathways for river discharged fresh water in the northern Gulf of Mexico. *Journal of Geophysical Research*, *108*, 3303. https://doi.org//10.1029/2002JC001674
Oey, L. Y., Ezer, T., Forristall, G., Cooper, C., DiMarco, S., & Fan, S. (2005). An exercise in forecasting loop current and eddy frontal positions in the Gulf of Mexico. *Geophysical Research Letters*, *32*, L12611. https://doi.org//10.1029/2005GL023253
Okubo, A. (1970). Horizontal dispersion of floatable particles in the vicinity of velocity singularities such as convergences, *Deep sea research and oceanographic abstracts* (Vol. 17, pp. 445–454). https://doi.org//10.1016/0011-7471(70)90059-8
Olson, D. B. (1986). Lateral exchange within Gulf Stream warm-core ring surface layers. *Deep Sea Research A*, *33*(11-12), 1691–1704. https://doi.org//10.1016/0198-0149(86)90074-9
Olson, D. B., & Evans, R. H. (1986). Rings of the Agulhas current. *Deep Sea Research Part A. Oceanographic Research Papers*, *33*(1), 27–42.
Putrasahan, D. A., Le Hénaff, M., & Kirtman, B. P. (2017). Importance of ocean mesoscale variability for air-sea interactions in the Gulf of Mexico. *Geophysical Research Letters*, *44*, 6352–6362. https://doi.org//10.1002/2017GL072884
Qiu, B., Chen, S., & Hacker, P. (2007). Effect of mesoscale eddies on subtropical mode water variability from the Kuroshio Extension System Study (KESS). *Journal of Physical Oceanography*, *37*(4), 982. https://doi.org//10.1175/JPO3097.1
Richardson, P. L. (1983). Gulf stream rings, *Eddies in marine science* (pp. 19–45): Springer.
Sasaki, Y. N., & Minobe, S. (2014). Climatological mean features and interannual to decadal variability of ring formations in the Kuroshio Extension Region (*OS41F-07*): AGU Fall Meeting Abstracts.
Shay, L. K., Goni, G. J., & Black, P. G. (2000). Effects of a warm oceanic feature on Hurricane Opal. *Monthly Weather Review*, *128*, 1366. https://doi.org//10.1175/1520-0493(2000)128<1366:EOAWOF>2.0.CO;2
Shcherbina, A. Y., Sundermeyer, M. A., Kunze, E., D'Asaro, E., Badin, G., Birch, D., & Ledwell, J. R. (2015). The LatMix summer campaign: Submesoscale stirring in the upper ocean. *Bulletin of the American Meteorological Society*, *96*, 1257–1279. https://doi.org//10.1175/BAMS-D-14-00015.1
Sheinbaum, J., Candela, J., Badan, A., & Ochoa, J. (2002). Flow structure and transport in the Yucatan Channel. *Geophysical Research Letters*, *29*(3), 1040. https://doi.org//10.1029/2001GL013990
Wang, Y., Beron-Vera, F. J., & Olascoaga, M. J. (2016). The life cycle of a coherent Lagrangian Agulhas ring. *Journal of Geophysical Research: Oceans*, *121*, 3944–3954. https://doi.org/10.1002/2015JC011620
Weiss, J. (1991). The dynamics of enstrophy transfer in two-dimensional hydrodynamics. *Physica D Nonlinear Phenomena*, *48*(2-3), 273–294. https://doi.org//10.1016/0167-2789(91)90088-Q
Willis, J. K., Roemmich, D., & Cornuelle, B. (2003). Combining altimetric height with broadscale profile data to estimate steric height, heat storage, subsurface temperature, and sea-surface temperature variability. *Journal of Geophysical Research*, *108*, C9. https://doi.org/10.1029/2002JC001755
Willis, J. K., Roemmich, D., & Cornuelle, B. (2004). Interannual variability in upper ocean heat content, temperature, and thermosteric expansion on global scales. *Journal of Geophysical Research*, *109*, C12036. https://doi.org/10.1029/2003JC002260
Yablonsky, R. M., & Ginis, I. (2013). Impact of a warm ocean eddy's circulation on hurricane-induced sea surface cooling with implications for hurricane intensity. *Monthly Weather Review*, *141*, 997–1021. https://doi.org//10.1175/MWR-D-12-00248.1
Zavala-Hidalgo, J., Perés-Sierra, A., & Ochoa, J. (2002). Seasonal variability of the temperature and heat fluxes in the Gulf of Mexico. *Atmósfera*, *15*(2), 81–104.
Zhurbas, V., & Oh, I. S. (2004). Drifter-derived maps of lateral diffusivity in the Pacific and Atlantic Oceans in relation to surface circulation patterns. *Journal of Geophysical Research*, *109*, C05015. https://doi.org//10.1029/2003JC002241